Chapter 5

Exploring Breakup Coupling Effect in ^{7}Li+^{92,100}Mo Elastic Scattering around Coulomb Barrier Energies

5.1 Introduction

5.2 Experimental setup

5.3 Experimental and Theoretical analysis

5.3.1 Optical Model Analysis

5.3.1.1 Wood-Saxon Potential (WSP) model analysis

5.3.1.2 São-Paulo Potential (SPP) model analysis

5.3.2 Dispersion Calculation

5.3.3 CDCC Analysis

5.4 Comparative studies of fusion and total reaction cross section

5.5 Summary and Conclusion

5.1 Introduction

The studies involving elastic /inelastic scattering, complete/incomplete fusion and, breakup followed by transfer near the Coulomb barrier region provide meaningful insight into reactions induced by Weakly Bound Projectiles (WBP) and Radioactive Ion Beams (RIBs). A Threshold Anomaly (TA) is an ubiquitous property of strongly bound nuclei in the barrier region. Whereas in loosely bound nuclei, a variety of behavior is reported at the barrier. ^{9}Be (breakup threshold 1.57 MeV) with ^{80}Se [1] and ^{197}Au [2] show Breakup Threshold Anomaly (BTA). ^{6}Li (breakup threshold 1.47 MeV) demonstrates BTA with nearly all the systems ^{27}Al [3], ^{80}Se [4], ^{112,116}Sn [5], ^{144}Sm [6], ^{208}Pb [7], ^{232}Th [8] but no strong BTA behavior with ^{28}Si [9, 10]. But in the case of ^{7}Li (breakup threshold 2.47 MeV, one bound excited state at 0.478 MeV), no static observation is reported. TA is observed for ^{7}Li with ^{59}Co [11], ^{80}Se [4], ^{138}Ba [12], ^{208}Pb [13], and ^{232}Th [8] whereas no TA was reported for ^{27}Al [14, 15], ^{28}Si [16], ^{116}Sn [17], ^{144}Sm [6], ^{159}Tb [18]. Moreover, lighter mass WBPs are still away from any general framework of TA/BTA and very few measurements are taken with ^{6}He, ^{8}B, and ^{7}Be. Thus perhaps a systematic behavior for ^{7}Li might be affected by a competition created by (1) bound inelastic state for attractive polarization potential and (2) breakup for repulsive polarization potential and the overall competition rely on the target [19]. The complexity of reaction studies requires a rich data library [20]. Concerning the above reports, the present work comprises the breakup reaction dynamics of WBP ^{7}Li on middle mass targets ^{92}Mo and ^{100}Mo [21].

5.2 Experimental setup

The present work was carried out using 15 UD Pelletron accelerator at Inter University Accelerator Centre (IUAC), New Delhi, India and beam aligned at General Purpose Scattering Chamber (GPSC) facility. The schematic layout of the accelerator is described in chapter 2 (section 2.1) with a detailed description of the accelerator's functioning. The measurement was done using a $^{7}Li^{3+}$ ion beam on self-supported ^{92,100}Mo targets. The targets used were 99.05% enriched and of thickness 217 μg/cm^2 and 305μg/cm^2 respectively, deposited on carbon backing of thickness ~22μg/cm^2. The incident energies for ion were 35, 30, 25, 23, 21.5, 19, 17.5, and 15 MeV, with current ~ 5-28 nA. A rectification of beam energies for half thickness of target were performed during scrutiny. This accounts for a deduction of ∼40 keV to ∼70 keV for 35 MeV to 15 MeV energy range for ^{92}Mo. Same way ∼50 keV at 35 MeV and ∼90 keV at 15 MeV for ^{100}Mo. ΔE+E telescope with seven silicon surface barrier detectors setup was operated for covering 15° to 168° angular range. Figure 5.1 shows the experimental arrangement of detectors and other components. Figure 5.2 depicts the internal view of the experimental arrangement of the chamber. . For beam monitoring and absolute normalization, 300 μm thick two surface barrier monitor detectors were mounted at ±10°. The detectors used, T1 having ΔE=40μm and E=2 mm, T2 with ΔE=40μm and E=1 mm, T3, T4, T5 detectors had ΔE=25μm and E=1 mm, T6 and T7 with ΔE=25μm and E=300 μm. T1-T5 detectors were kept at a rotating arm with 6° separation between each and T6 and T7 were fixed at back angles 156° and 168°. Each detector is collimated and thus covers an angle between 0.9 msr to 6 msr. The data were recorded using

the software FREEDOM [22] and analyzed using the Linux-based data acquisition system LAMPS [23]. Figure 5.3 shows a typical particle spectrum for $^{7}Li+^{92}Mo$ system at E_{lab}=35 MeV and lab angle 27°.

5.3 Experimental and Theoretical analysis

Two distinct models were used to analyze the angular distribution of elastic scattering., double folding São-Paulo potential (SPP) and Woods-Saxon potential (WSP). Phenomenological fits are employed to determine the potential parameters which have a dependence on energy, and this information is utilized to establish the 'Sensitivity Radius'. Impact caused by breakup at time of reaction is investigated using theoretical CDCC calculations.

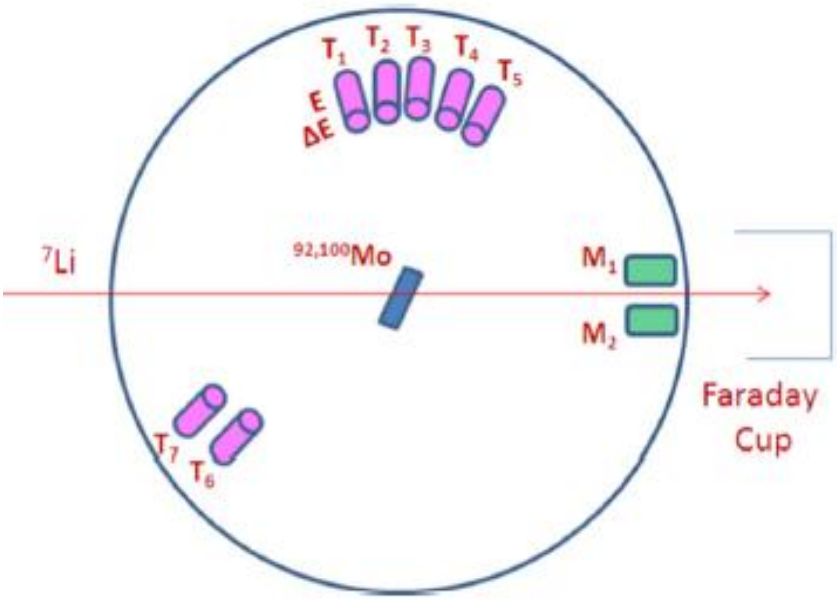

igure 5.1: *Schematic diagram of the GPSC chamber of the experimental setup for the experiment.*

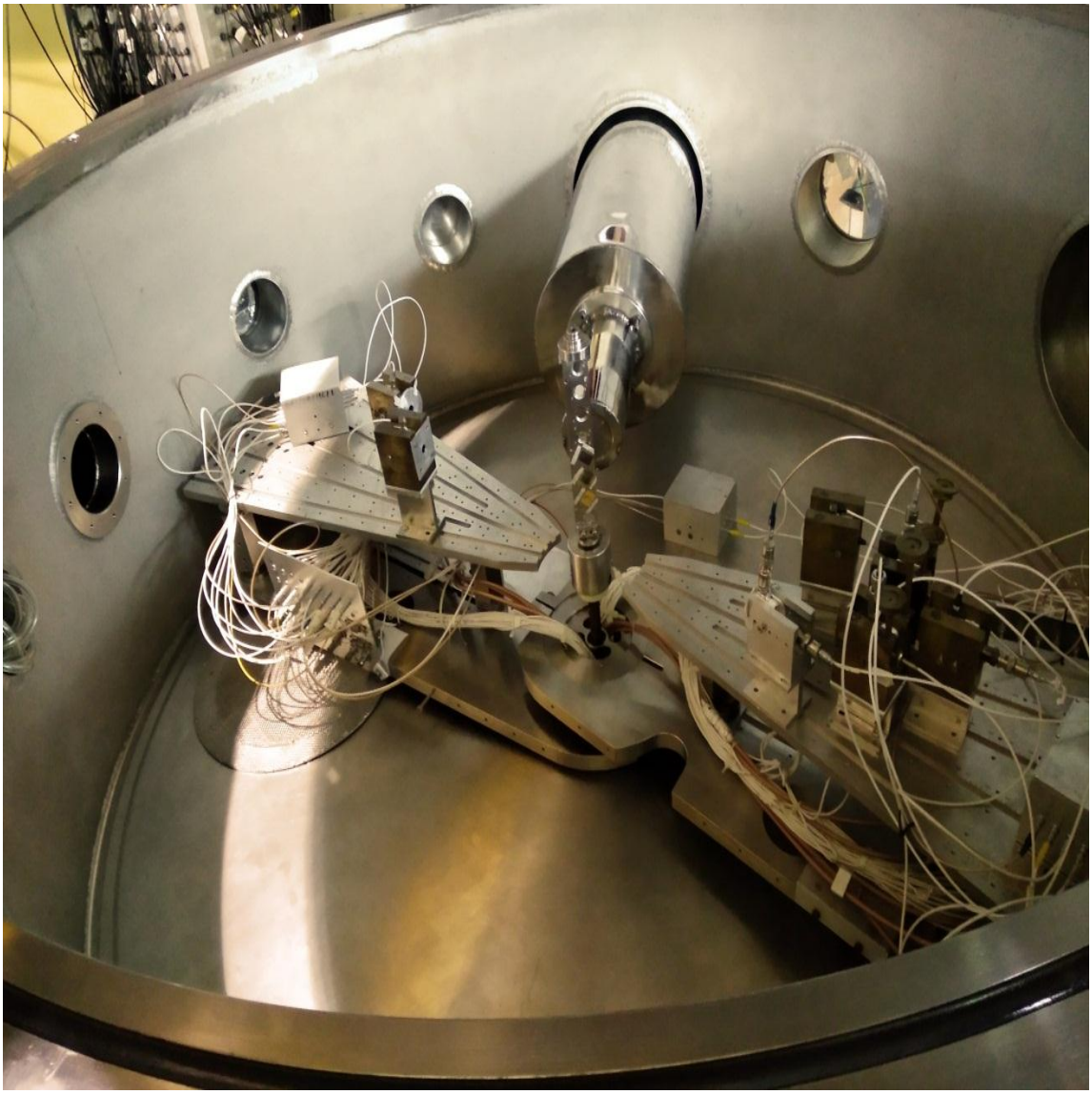

Figure 5.2: *Schematic diagram of the inner view of GPSC chamber of the experimental setup for the experiment.*

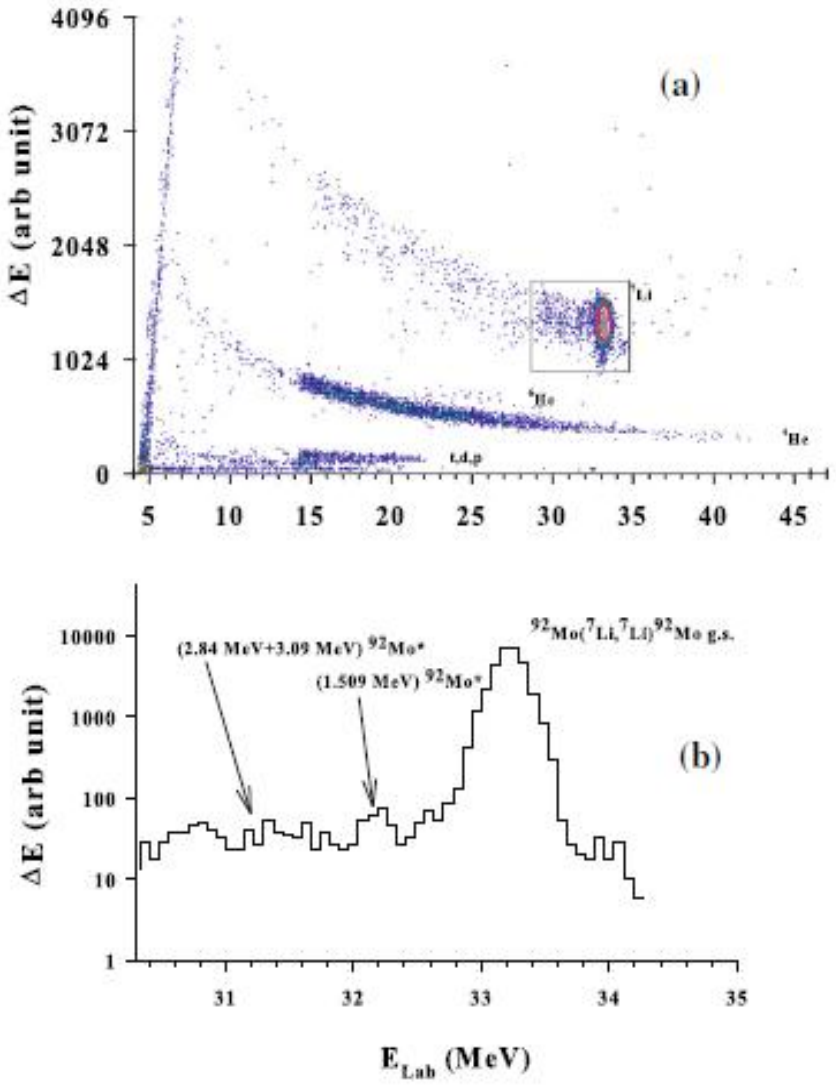

Figure 5.3: *An energy calibrated experimental spectra* ***(a)*** *for the system* $^{7}Li+^{92}Mo$ *at energy* E_{lab} *= 35 MeV and* θ_{lab} *= 27°;* ***(b)*** *the projection of the drawn box reveals the first few inelastic states of target* ^{92}Mo.

5.3.1 Optical Model Analysis

5.3.1.1 Wood-Saxon Potential (WSP) model analysis

Using the SFRESCO module of the FRESCO program, version 3.1, the elastic scattering data was examined [24]. The total potential is given as the sum of Coulomb and nuclear potential as following-

$$V(r, E) = V_C® + \frac{-V0}{1+\exp(r-Rv)/av} + i \frac{-W0}{1+\exp(r-Rw)/aw} \quad (4.1)$$

Here, V_C (r) is Coulomb potential, $Rv = r_v (A_P^{(1/3)} + A_T^{(1/3)})$ and $Rw = r_w (A_P^{(1/3)} + A_T^{(1/3)})$, A_P and A_T are masses of projectile and target respectively. The depths of potential (V_0, W_0), geometrical parameters (r_v, r_w), and diffuseness parameters (a_v, a_w) for real and imaginary components were all altered in simultaneously to find the parameters that best suit the experimental results. The Akyüz-Winther potential served as the source for the initial depth parameters for fitting. [25]. The search for parameters was within χ^2/N range $\chi 2 = \chi 2_{min} + \chi 2_{min}/2$. The errors obtained in reaction cross sections and fittings are decided by acceptable ranges. The obtained best fitted values are given in Tables 5.1 and 5.3. The corresponding angular distribution is presented in figure 5.4 (a) in blue solid lines. The fitting procedure is further used to calculate the absorption radius (or radius of sensitivity) also for both potential. Obtained diffuseness parameter is varied in the difference of some fixed steps around the best fit values to obtain a family of curves satisfying potential parameters. The crossing point of these curves gives the radius of sensitivity. The average sensitivity radius calculated was ~ 9.58 fm for

^{7}Li+^{92}Mo and ~10.28 fm for ^{7}Li+^{100}Mo systems. The corresponding plot of the sensitivity radius for the ^{7}Li+^{100}Mo system is given in figure 5.5 (a) and (b) for the real part at energy 21.5 MeV and the imaginary part at 30 MeV. Calculation of potential parameter energy dependency at this sensitivity radius using the dispersion relation [26].

5.3.1.2 São-Paulo Potential (SPP) model analysis

In the analysis of SPP, we assumed a normalized formulation of optical potential as follows-

$$V_{SPP}(R, E) = (N_R(E) + i\, N_I(E))\, V_N(R,E) \qquad (4.2)$$

The effects of the dynamic polarisation potential (DPP) caused by direct channel couplings are taken into consideration by normalization factors N_R and N_I [27].These factors are obtained by χ^2 minimization in fitting to the experimental measurements and are done by with help of FRESCO code [24]. The angular distribution of calculations is given in figure 5.4 (a) and (b) in pink dashed for systems ^{7}Li+^{92}Mo and ^{7}Li+^{100}Mo. It can be observed that fitting is not much different from WSP fittings and obtained parameters with cross sections are remarked in Tables 5.2 and 5.4.

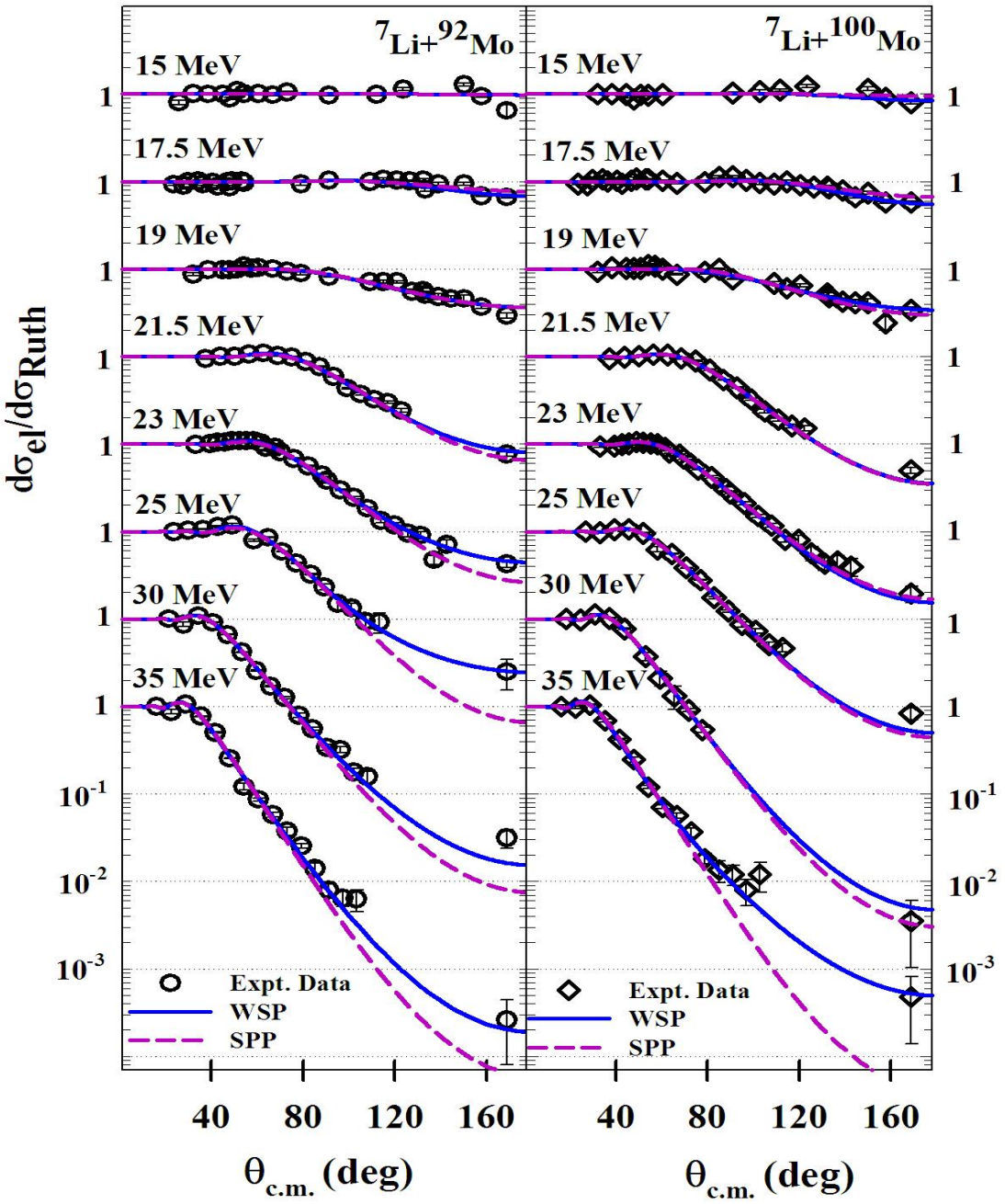

Figure 5.4: *Elastic scattering angular distribution data fitting through Woods –Saxon potential (WSP) and São-Paulo Potential (SPP). Circles are experimental data points for system $^{7}Li+^{92}Mo$ and diamonds for system $^{7}Li+^{100}Mo$.*

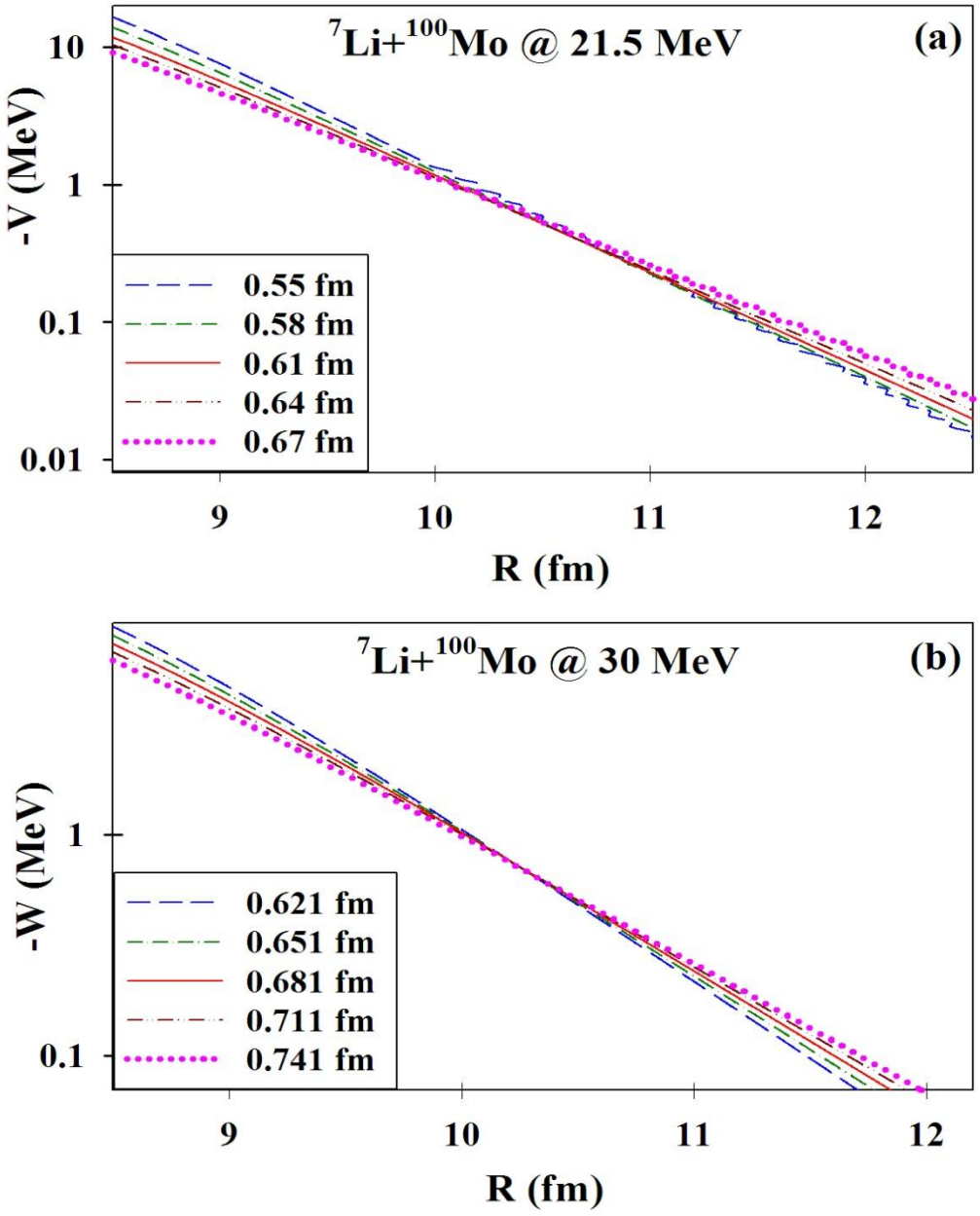

Figure 5.5: *The sensitivity radius deduced from optical model analysis for the real and imaginary parts for the system $^{7}Li+^{100}Mo$ system at energies 21.5 MeV and 30 MeV respectively.*

Table 5.1

Best fit optical potential parameters from elastic scattering data and N represents the number of data points for the system $^{7}Li+^{92}Mo$.

E_{lab} (MeV)	V0 (MeV)	r_v (fm)	av (fm)	W_0 (MeV)	R_w (fm)	aw (fm)	σ_R (mb)	X^2/N
34.96	59.03	1.24	0.44	25.00	1.10	0.79	1573	5.2
29.96	40.00	1.12	0.53	35.26	1.16	0.69	1250	13.6
24.95	35.00	1.10	0.78	41.96	1.19	0.43	660	8.1
22.95	40.49	1.11	0.77	33.78	1.24	0.49	610	3.3
21.45	40.00	1.10	0.79	47.66	1.17	0.49	407	5.1
18.94	53.75	1.10	0.54	57.96	1.10	0.78	321	5.9
17.44	40.00	1.13	0.79	25.00	1.10	0.45	23	7.7
14.93	49.85	1.25	0.59	5.00	1.10	0.34	0.76	6.8

Table 5.2

The normalization factors N_R and N_I for real and imaginary parts of the SPP were determined with SFRESCO for the system $^{7}Li+^{92}Mo$.

E_{lab} (MeV)	N_R	N_I	X^2/N	σ total (mb)
34.96	0.616	1.144	9.89	1570
29.96	0.211	1.087	5.29	1237
24.95	0.486	0.438	9.24	743
22.95	0.616	0.748	7.85	659
21.45	0.658	0.528	7.5	454
18.94	0.342	1.990	6.0	306
17.44	0.850	0.130	10.5	26
14.93	1.850	0.100	6.8	0.8

Table 5.3

Best fit optical potential parameters from elastic scattering data and N represents the number of data points for the system $^{7}Li+^{100}Mo$.

E_{lab} (MeV)	V0 (MeV)	r_v (fm)	av (fm)	W_0 (MeV)	R_w (fm)	aw (fm)	σ_R (mb)	X^2/N
34.96	40.08	1.10	0.79	72.94	1.18	0.55	1623	2.8
29.96	25.00	1.10	0.839	30.00	1.17	0.681	1363	3.9
24.95	45.10	1.10	0.73	63.75	1.10	0.69	1036	3.1
22.95	32.37	1.19	0.52	15.00	1.10	0.84	792	1.8
21.45	79.20	1.14	0.61	28.00	1.10	0.75	614	4.0
18.94	35.77	1.10	0.45	36.47	1.15	0.79	359	10.7
17.44	28.31	1.24	0.67	49.99	1.18	0.35	53	5.5
14.93	39.99	1.25	0.85	6.76	1.1	0.35	8.7	8.7

Table 5.4

The normalization factors N_R and N_I for real and imaginary parts of the SPP were determined with SFRESCO for the system $^{7}Li+^{100}Mo$.

E_{lab} (MeV)	N_R	N_I	X^2/N	σ total (mb)
34.96	0.614	1.139	4.96	1670
29.96	0.656	0.996	4.8	1380
24.95	0.796	1.126	5.0	1043
22.95	0.777	1.184	2.6	844
21.45	0.849	0.766	4.27	611
18.94	0.500	1.500	11.0	311
17.44	0.900	0.120	11.33	45
14.93	2.000	0.100	10.89	3.7

5.3.2 Dispersion Calculation

Using the dispersion relation, the energy dependence of the optical potential parameters is computed at the sensitivity radius [26]. Utilizing the dispersion relation, it is possible to identify the interdependence of real and imaginary potentials [27] as follows:

$$V(r, E) = V_0(r, E) + \Delta V(r, E)$$

and

$$\Delta V(r, E) = \frac{P}{\pi} \int_0^{\infty} \frac{W(r,E')}{E'-E}\, dE' \qquad (5.3)$$

ΔV (r, E) turns attractive polarization potential and depends on imaginary potential W (r, E') (detailed description is given in chapter 2 (section 2.3)) whose form is presumptively composed of two or three segments, and correlated real potential is determined using calculations of the dispersion relation. Figures 5.6 and 5.7 show outcomes of the dispersion relation for systems ^{7}Li+^{92}Mo and ^{7}Li+^{100}Mo respectively. Concurrently, panels (a) and (b) depict results related to WSP and panels (c) and (d) to SPP. Careful observation of both figures 5.6 (a), (b) and 5.7 (a), (b) reveals that the two segment breakage of an imaginary part does not define the experimental real part well but instead three segments are producing a better definition for the real potential. Thus Threshold Anomaly (TA) corresponding to two segments is absent and Breakup Threshold Anomaly (BTA) can be observed for both systems. A similar observation of BTA can be clarified from the calculations of normalization parameters N_R and N_I from SPP. Thus imaginary part increases before decreasing in the adjacent of barrier and producing a corresponding lowering in real potential notifying BTA behavior in the Coulomb barrier region for ^{7}Li+^{92}Mo and ^{7}Li+^{100}Mo systems.

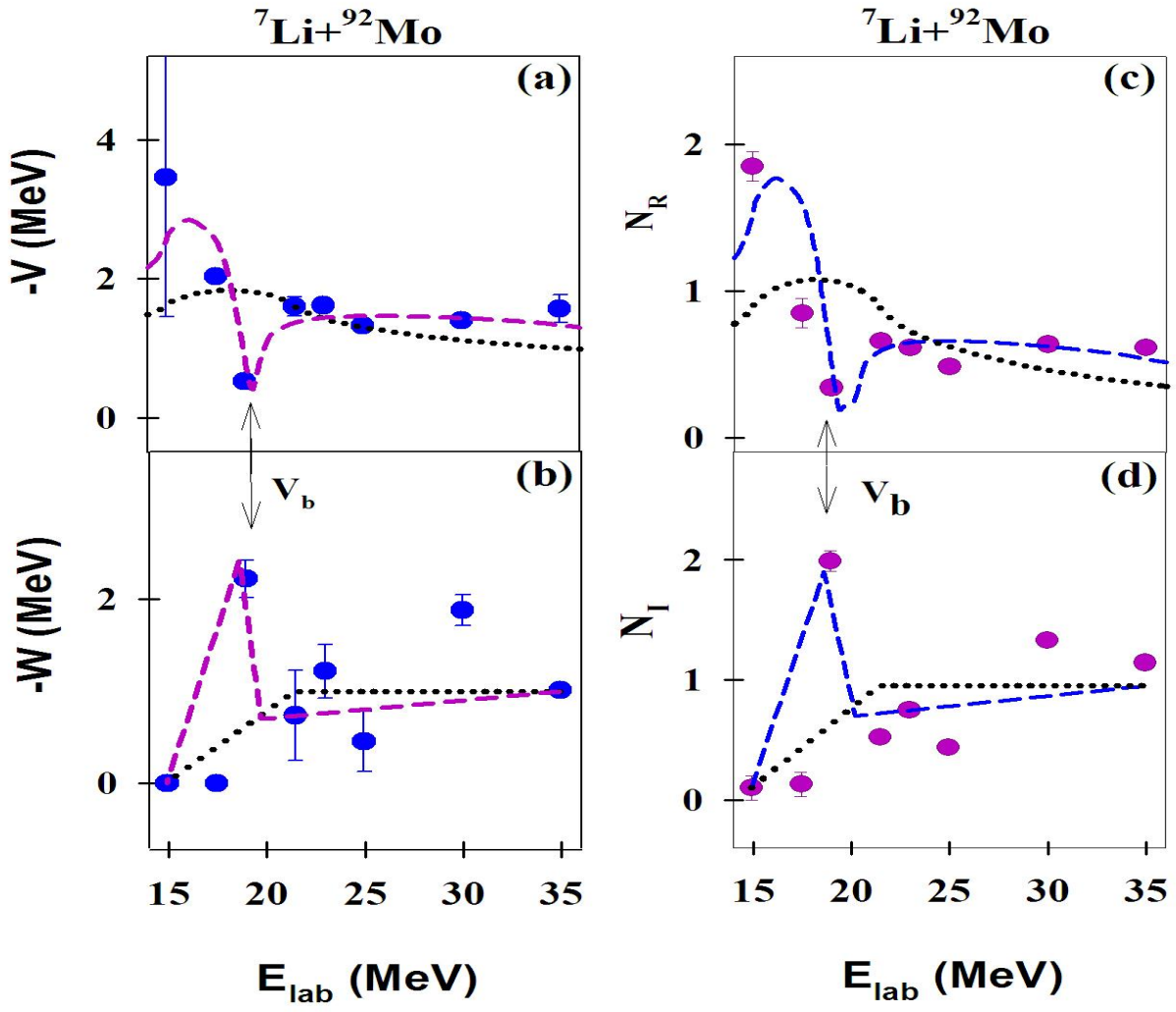

Figure 5.6: *Left panel: Real and imaginary potentials at sensitivity radius R=9.58 fm using optical model WSP (blue solid circle). Right panel: Real and imaginary potentials at sensitivity radius using optical model SPP (pink solid circle). The dotted line represents two segment dispersion calculations and the dashed line shows three segment dispersion calculations for system* $^{7}Li+^{92}Mo$.

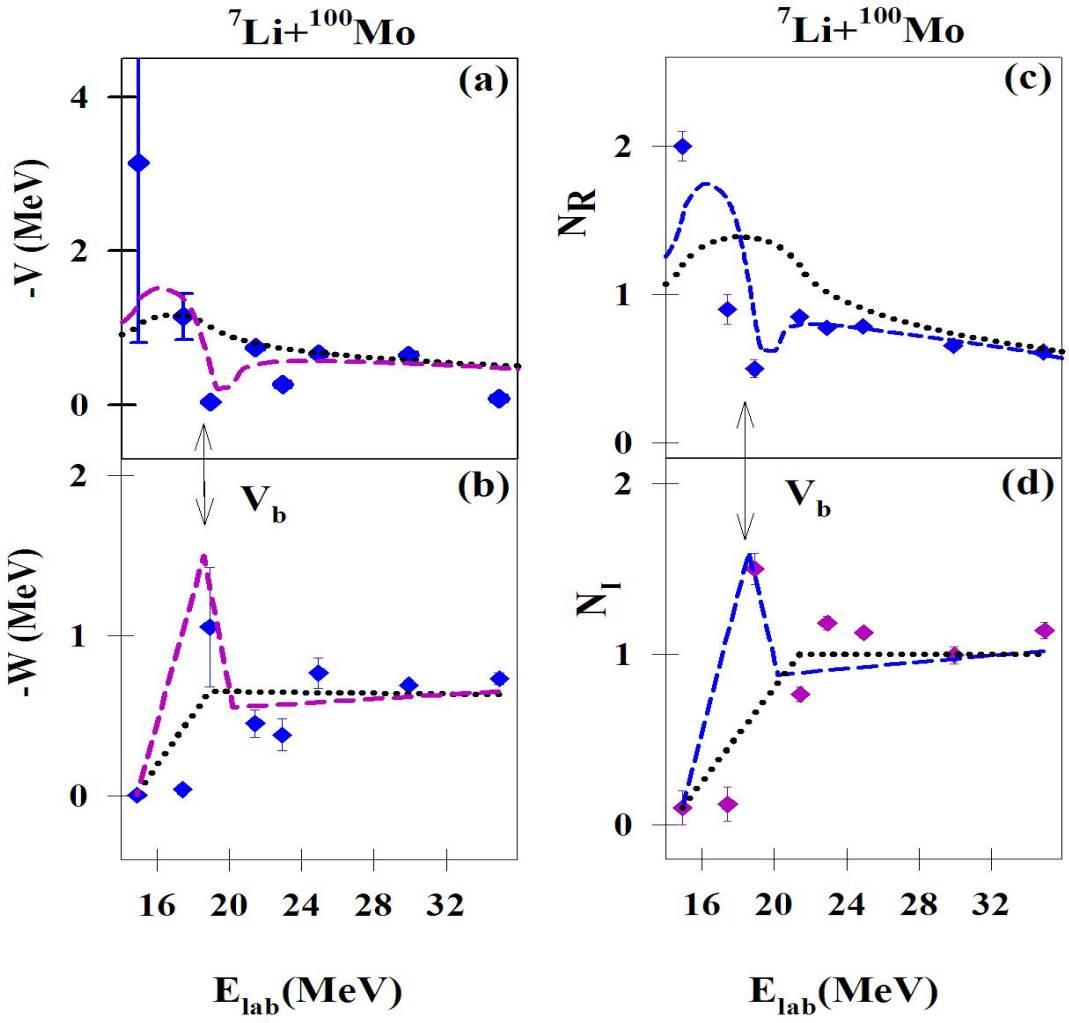

Figure 5.7: *Left panel: Real and imaginary potentials at sensitivity radius R=10.28 fm using optical model WSP (blue solid circle). Right panel: Real and imaginary potentials at sensitivity radius using optical model SPP (pink solid circle). The dotted line represents two segment dispersion calculations and the dashed line shows three segment dispersion calculations for system* $^{7}Li+^{100}Mo$.

5.3.3 CDCC Analysis

CDCC calculations play a significant role to explore the breakup coupling effects of $^{7}Li \rightarrow \alpha + t$, by practicing the FRESCO code of version 3.1 [24]. Below the breakup threshold of ~ 2.45 MeV, a bound energy state of 0.477 MeV ($j = ½^-$, l=1) exist for the ^{7}Li projectile, and this state is included in calculations along with ground state ($j = 3/2^-$, l=1). Above 2.45 MeV, the continuum was discretized into equal momentum bins. For all projectile states, the binding potentials between α + t clusters were derived from references [28]. The discretization for momentum was continued up to excitation energy 10 MeV and corresponding bins had angular momenta up to $l = 3\hbar$. The potential for real part of projectile fragment and target was considered from São- Paulo potential and the imaginary part was obtained by multiplication of 0.78 to real one. A very good convergence to the experimental data is shown in figures 5.8 and 5.9 give the demonstration of a compatible explanation of experimental data with CDCC calculations. We can observe that dashed blue line calculations with breakup coupling are in concurrence with data in comparison to orange dashed lines for calculations without breakup coupling. Well, the difference is marginal between the two modes of calculations but such effects are pronounced more in projectiles like ^{6}Li possibly due to their low breakup threshold.

The cross section obtained by phenomenological calculations is compared with theoretical CDCC calculations in figure 5.10 for the system $^{7}Li+^{92,100}Mo$. The cross section for ^{100}Mo is than to ^{92}Mo. The consequence of breakup cross section is pronounced more near the barrier region and also breakup coupling pronounces more its effect on ^{100}Mo compared to ^{92}Mo.

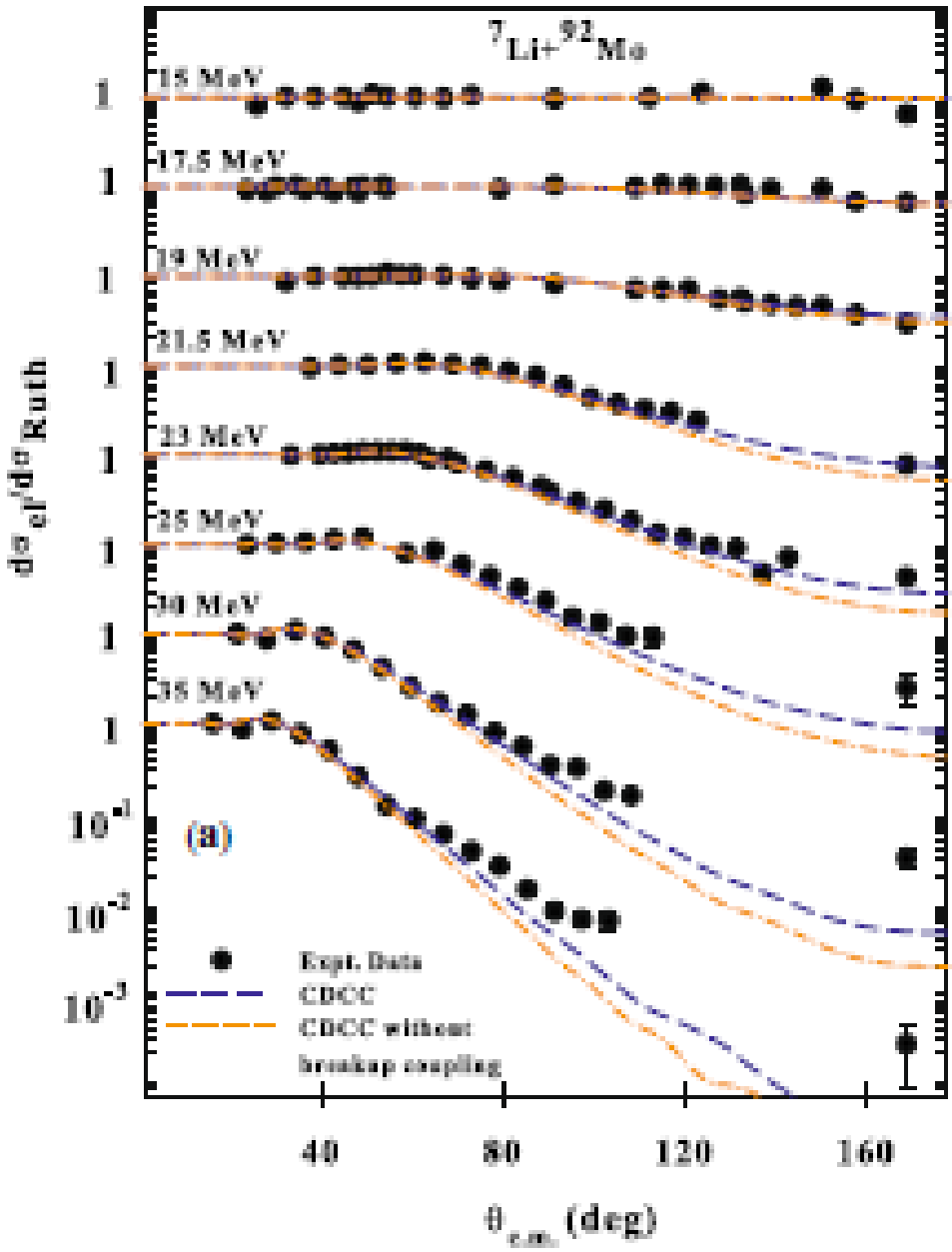

Figure 5.8: *The CDCC calculations are demonstrated with and without including breakup coupling effects. Blue dashed lines represent the result of calculations with breakup (BU) effects and orange dashed dot lines without BU effects for the system* $^{7}Li+^{92}Mo$.

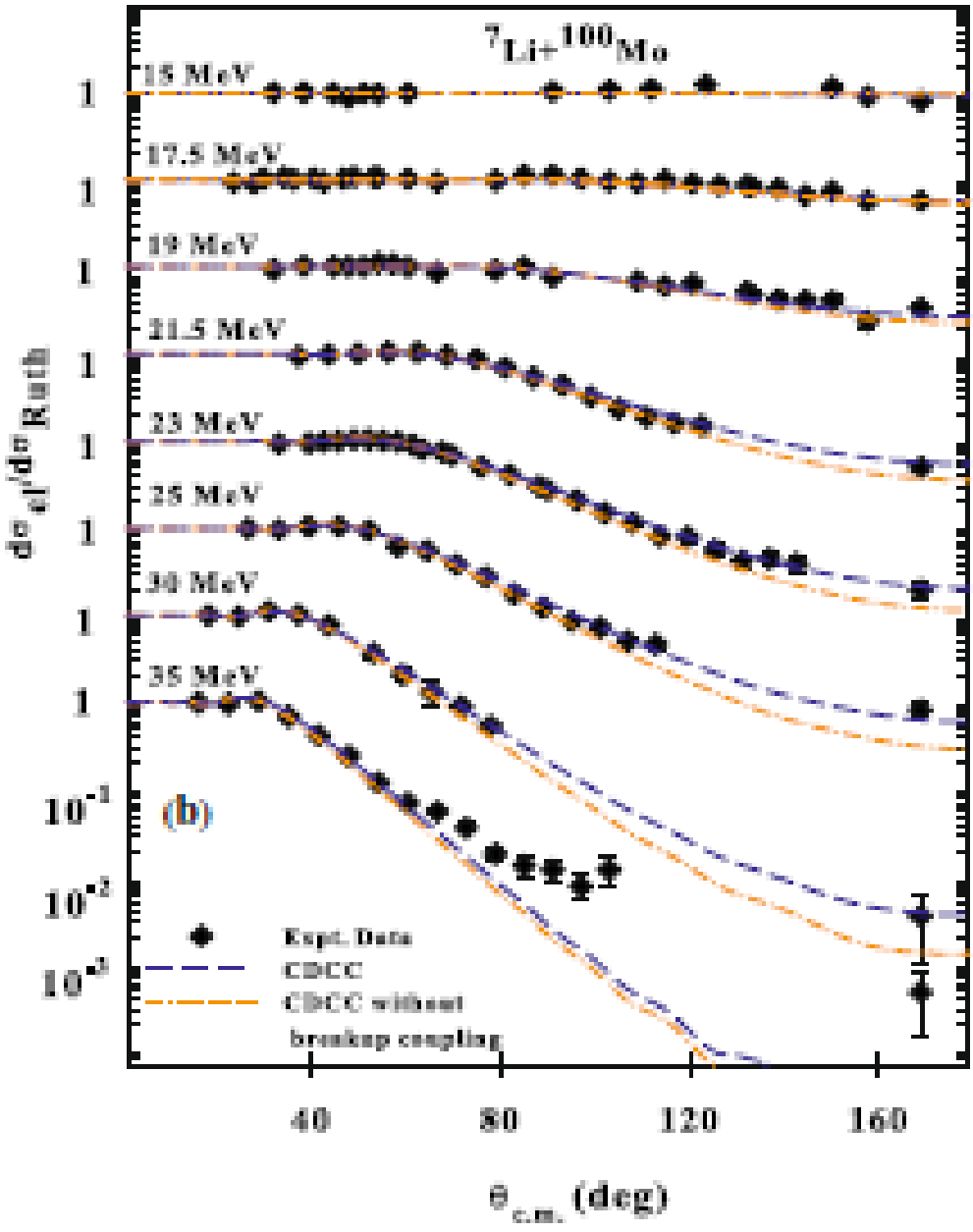

Figure 5.9: *The CDCC calculations are demonstrated with and without including breakup coupling effects. Blue dashed lines represent the result of calculations with breakup (BU) effects and orange dashed dot lines without BU effects for the system* $^{7}Li+^{100}Mo$.

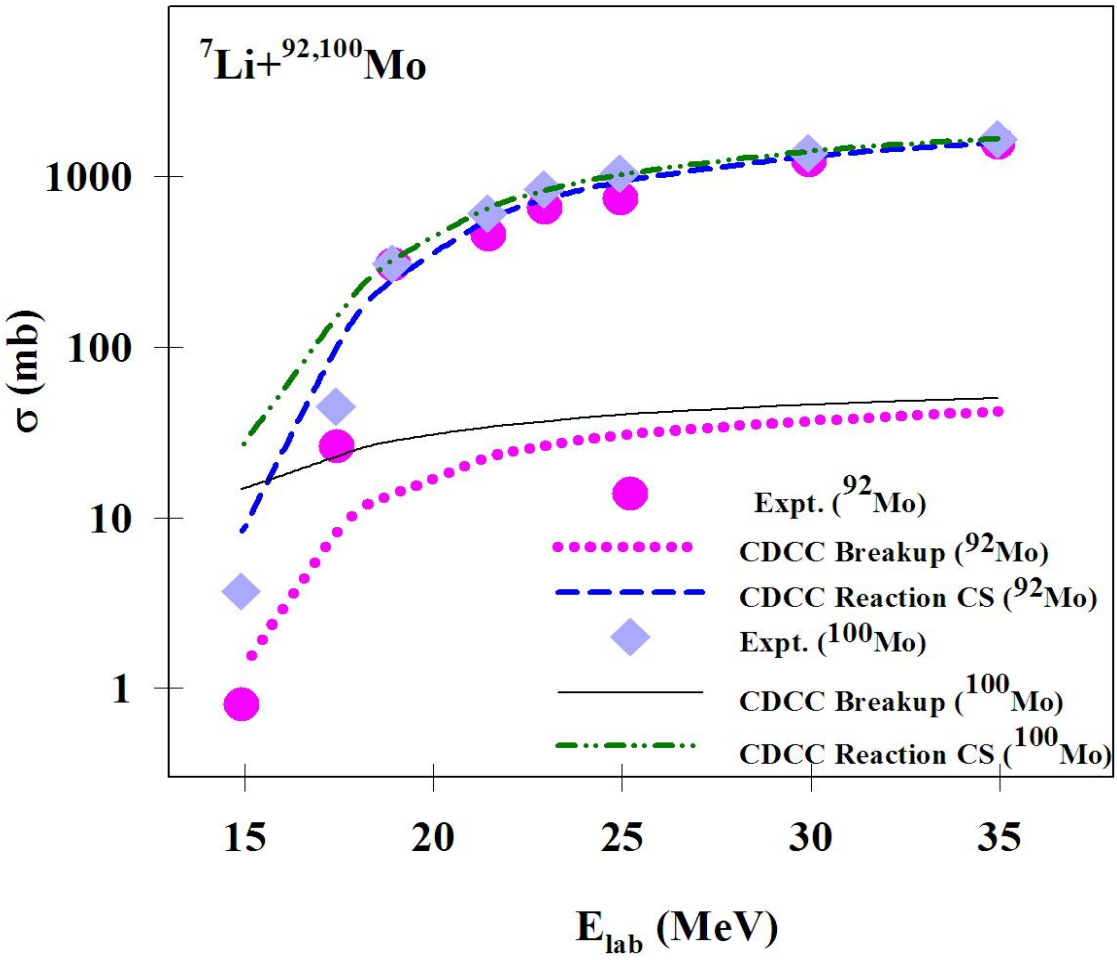

Figure 5.10: *A Comparative study of the experimental cross section with CDCC calculated reaction cross section and breakup cross section for $^{7}Li+^{92,100}Mo$ systems. The pink circles (^{92}Mo) and light blue diamond boxes (^{100}Mo) designate experimental points. The reaction cross section from CDCC calculations are in blue dashed (^{92}Mo) and green dash-dot-dot (^{100}Mo) lines. CDCC calculated breakup cross sections are shown in pink dotted line (^{92}Mo) and solid black line (^{100}Mo) respectively.*

5.4 Comparative studies of fusion and total reaction cross section

This is one of the methods to inspect the impact of breakup channel on the fusion of weakly bound systems [39]. Using the coupled channel code CCFULL, the fusion cross sections for the systems ^{7}Li+^{92,100}Mo and ^{6}Li+^{100}Mo have been determined [35]. This calculation takes into account energy ranging from 14 MeV to 35 MeV in 1 MeV step size, target excitation level to be included E* with quadrupole deformation parameter β2 for respective the target (^{92}Mo or ^{100}Mo), potential parameters (V0,r, a) for the system which were taken from fitted elastic scattering data corresponding to system. In above work, Total reaction cross sections for the systems ^{7}Li+^{92,100}Mo derived from the aforementioned experimental elastic scattering study and for ^{6}Li+^{100}Mo have been computed and are shown in the following chapter 6. A comparative study is performed for fusion cross section and total reaction cross section and presented in figure 5.11. The strong enhancement of total fusion for above barrier energies can be noted compared to below barrier energies. Total reaction cross sections for ^{7}Li+^{92}Mo observed to be marginally higher than calculated fusion cross sections for system. The total reaction cross sections for ^{7}Li+^{100}Mo show dominance of total cross section compared to fusion cross section in the sub-barrier energy region. This might imply that the persistent differences were because of dynamic channel coupling effects, primarily with a noteworthy contribution from the breakup channel. The dominance of reaction cross section over fusion can be observed for ^{6}Li+^{100}Mo system which is even larger than ^{7}Li. This might be a clue that ^{6}Li projectiles have a substantially higher inclusive breakup reaction cross section than ^{7}Li projectiles. Comparatively higher inclusive breakup reaction cross section of ^{6}Li projectile comprises of

favoring results of WBP dynamics are in a similarity to the work presented in earlier analysis in chapter 4 of the thesis, where large inclusive α cross sections indicate the breakup contribution to ^{6}Li induced reaction. The importance of projectile structure in reaction dynamics and the impact of breakup process in fusion cross section around the barrier energies have been studied for WBP and SBP [35-38]. Indeed, the experiment was designed and setup to understand elastic scattering, inclusive α- particle production studies, quasielastic scattering studies, fusion studies and charge particle production studies like p, d, t. The solid state detectors were capable to do the above studies and in the vision for fusion studies, we performed the experiment with installation of one HpGe detector at 90° angle in GPSC chamber to collect the characteristic γ - radiations. But the solid state detectors were showing lot of noise with HpGe in the chamber. Even the data with only HpGe in operation was also with non-conclusive quality. We are waiting for another beam time to get a good quality data with the system to understand the fusion dynamics in detailed. A systematic study of reaction cross section was carried out for light to heavier targets with ^{7}Li. To diminish the influence of charge and mass of participating nuclei, we adopt the reduction method as in reference [29]. The cross section is reduced to scale here σ_R for cross section, E for the energy of the projectile, Z for mass number, and T and P denote target and projectile individually. Figure 5.12 demonstrates the variation of the reduced cross section for mass range targets light to heavy with a weakly bound projectile. At lower energy regions mass dependency in light mass targets can be seen. Even though the masses of ^{92}Mo and ^{100}Mo are not much different from each other but still a marginal difference can be observed in their cross sections which possibly because of the comparatively larger deformation of ^{100}Mo than ^{92}Mo.

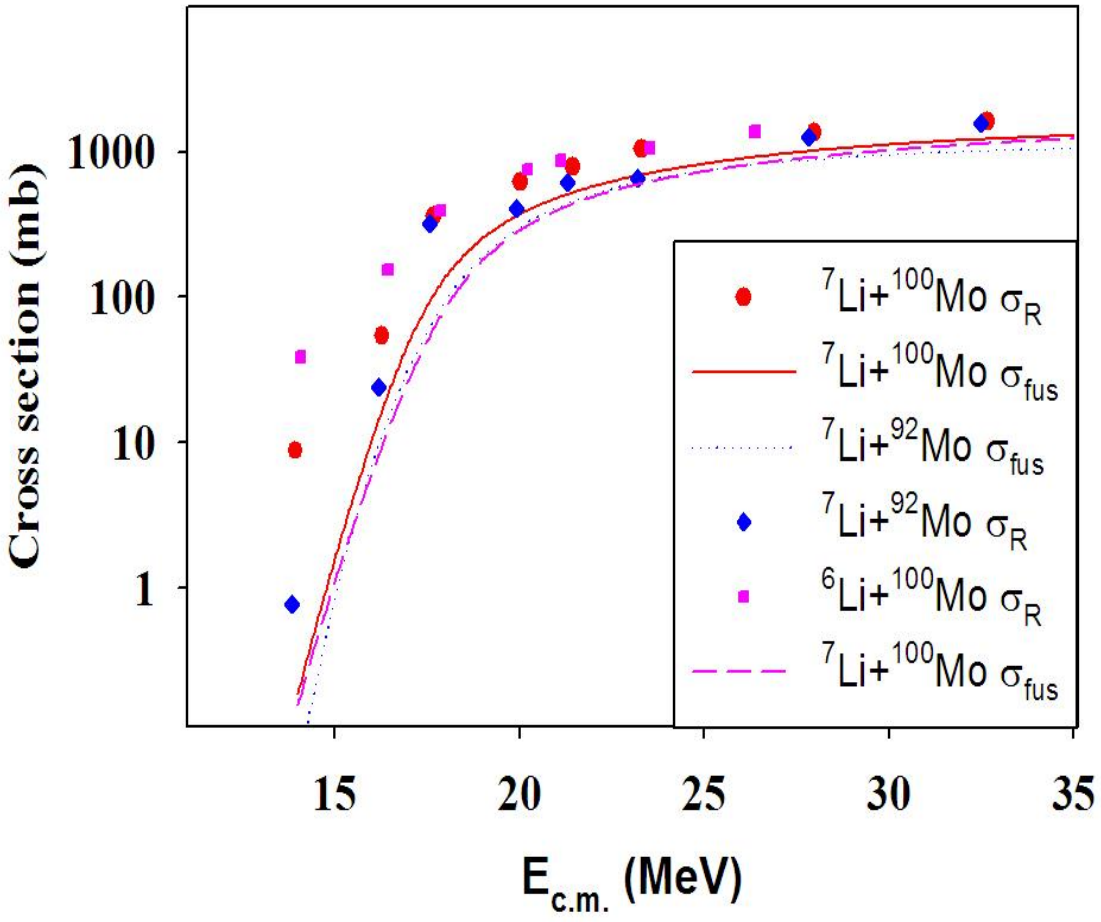

Figure 5.11: *The comparative plot for total fusion cross sections (σ_{fus}) calculated by CCFULL and the total reaction cross sections (σ_R) for the systems $^{7}Li+^{92}Mo$ (blue dashed line and diamonds respectively), $^{7}Li+,^{100}Mo$ (red solid line and circles respectively), and $^{6}Li+,^{100}Mo$ (pink dotted line and squares respectively).*

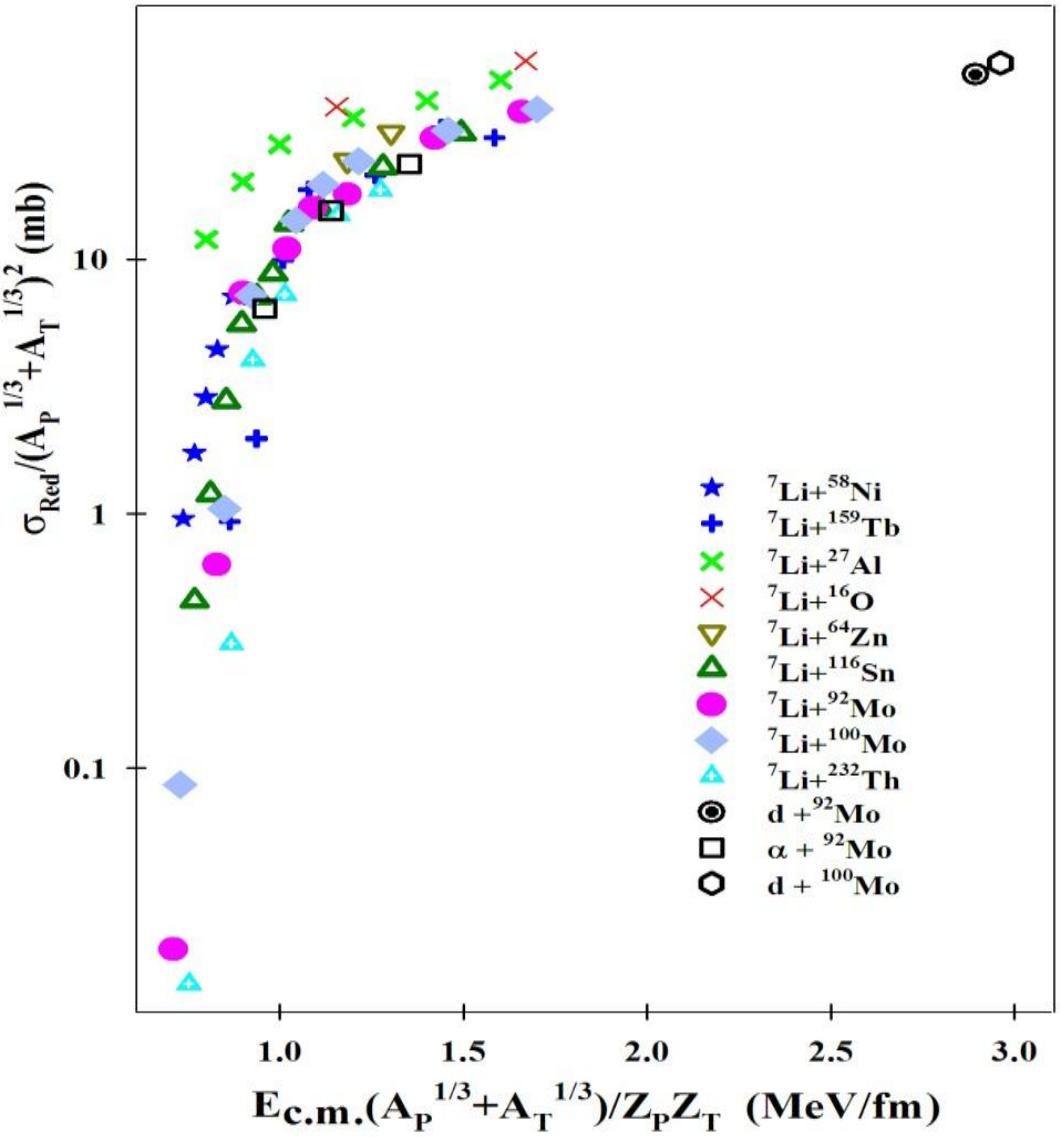

Figure 5.12: *Reduced reaction cross section for targets from lighter to heavy mass regions with ^{7}Li. The present system targets are indicated in the pink circle (^{92}Mo) and blue diamond (^{100}Mo) Reduction formulas for energy are mentioned on the axis. The cross sections are taken from reference [15, 18, 8, 30, 31, 32, 14]. The reaction cross section with d [33] and tightly bound α [34] are also shown.*

5.5 Summary and Conclusions:

In this chapter, we performed measurment for elastic scattering angular distribution for systems ^{7}Li+^{92,100}Mo around the Coulomb barrier energies. Using Woods-Saxon potential and São -Paulo potential, the experimental results were phenomenological analyzed. At sensitivity radii, the potential parameters are retrieved from optical model analysis and energy dependency of parameters are computed at that. The parameters show 'breakup threshold anomaly' nearby the Coulomb barrier. The same is confirmed from the study of normalization parameters derived from the São-Paulo potential model analysis. The breakup couplings effects were explored using Continuum Discretized Coupled Channels (CDCC) calculations on weakly bound projectile ^{7}Li states. And it was understood from the calculations that CDCC calculations with breakup coupling to the channels give a rich representation of experimental data in comparison to calculations without breakup coupling. The total reaction cross section compared to fusion probabilities show marginal dominance for ^{7}Li+^{92}Mo system, considerable dominance for ^{7}Li+^{100}Mo in sub-barrier energy region. This might imply that the persistent differences were caused by dynamic channel coupling effects, primarily with a noteworthy contribution from the breakup channel. The dominance of reaction cross section over fusion can be observed for ^{6}Li+^{100}Mo system which is even larger than ^{7}Li. A thorough analysis of the overall reaction cross section for various mass region targets using ^{7}Li indicates that the cross section is mass and shape dependent.

References

[1] F. Gollan, D. Abriola, A. Arazi, O.A. Capurro, M.A. Cardona, E. J.E. Testoni, Nucl. Phys. A **979**, 87 (2018).

[2] F. Gollan, D. Abriola, A. Arazi, M.A. Cardona, E. de Barbará, D. Hojman, R.M. Id Betan, G.V. Martí, A.J. Pacheco, D. Rodrigues, M. Togneri, Nucl. Phys. A **1000**, 121789 (2020).

[3] J.M. Figueira, J.O. Fernandez Niello, D. Abriola, A. Arazi, O.A. Capurro, E. d Barbará, G.V. Martínez, D.M. Heimann, A.E. Negri, A.J. Pacheco et al., Phys. Rev. C **75**, 017602 (2007).

[4] L. Fimiani, J.M. Figueira, G.V. Martí, J.E. Testoni, A.J. Pacheco, W.H.Z. Cárdenas, A. Arazi, O.A. Capurro, M.A. Cardona, P. Carnelli et al., Phys. Rev. C **86**, 044607 (2012).

[5] N.N. Deshmukh, S. Mukherjee, D. Patel, N.L. Singh, P.K. Rath, B.K. Nayak, D.C. Biswas, S. Santra, E.T.Mirgule, L.S. Danu et al., Phys. Rev. C **83**, 024607 (2011)

[6] J.M. Figueira, J.O. Fernandez Niello, A. Arazi, O.A. Capurro, P. Carnelli, L. Fimiani, G.V. Martí, D.M. Heimann, A.E. Negri, A.J. Pacheco et al., Phys. Rev. C **81**, 024613 (2010).

[7] M.S. Hussein, P.R.S. Gomes, J. Lubian, L.C. Chamon, Phys. Rev. C **73**, 044610 (2006)

[8] S. Dubey, S. Mukherjee, D.C. Biswas, B.K. Nayak, D. Patel, G.K. Prajapati, Y.K. Gupta, B.N. Joshi, L.S. Danu, S. Mukhopadhyay et al., Phys. Rev. C **89**, 014610 (2014)

[9] A. Pakou, N. Alamanos, A. Lagoyannis, A. Gillibert, E. Pollacco, P. Assimakopoulos, G. Doukelis, K. Ioannides, D. Karadimos, D. Karamanis et al., Phys. Lett. B **556**, 21 (2003)

[10] A. Pakou, N. Alamanos, G. Doukelis, A. Gillibert, G. Kalyva, M. Kokkoris, S. Kossionides, A. Lagoyannis, A. Musumarra, C. Papachristodoulou et al., Phys. Rev. C **69**, 054602 (2004)

[11] F.A. Souza, L.A.S. Leal,N. Carlin, M.G. Munhoz, R. LiguoriNeto, M. M. d Moura, A.A.P. Suaide, E.M. Szanto, ASd. Toledo, J. Takahashi, Phys. Rev. C **75**, 044601 (2007)

[12] A.M.M. Maciel, P.R.S. Gomes, J. Lubian, R.M.Anjos, R. Cabezas, G.M. Santos, C. Muri, S.B. Moraes, R.L. Neto, N. Added et al., Phys. Rev. C **59**, 2103 (1999)

[13] N. Keeley, S. Bennett, N. Clarke, B. Fulton, G. Tungate, P. Drumm, M. Nagarajan, J. Lilley, Nucl. Phys. A **571**, 326 (1994)

[14] J.M. Figueira, D. Abriola, J.O. Fernandez Niello, A. Arazi, O.A. Capurro, E. de Barbará, G.V. Martí, D. Martínez Heimann, A.J. Pacheco, J.E. Testoni et al., Phys. Rev. C **73**, 054603 (2006)

[15] D. Patel, S. Santra, S. Mukherjee, B.K. Nayak, P.K. Rath, V.V. Parkar, R.K. Choudhury, Pramana J. Phys. **81**, 587–602 (2013)

[16] A. Pakou, Phys. Rev. C **78**, 067601 (2008)

[17] N.N. Deshmukh, S. Mukherjee, B.K. Nayak, D.C. Biswas, S. Santra, E.T. Mirgule, S. Appannababu, D. Patel, A. Saxena, R.K. Choudhury et al., Eur. Phys. J. A **47**, 118 (2011)

[18] D. Patel, S. Mukherjee, D.C. Biswas, B.K.Nayak,Y.K.Gupta, L.S. Danu, S. Santra, E.T. Mirgule, Phys. Rev. C **91**, 054614 (2015)

[19] L. Fimiani, J.M. Figueira, G.V. Martí, J.E. Testoni, A.J. Pacheco, W.H.Z. Cárdenas, A. Arazi, O.A. Capurro, M.A. Cardona, P. Carnelli et al., Phys. Rev. C **86**, 044607 (2012) J. Lei, A.M. Moro, Phys. Rev. Lett. **122**, 042503 (2019) and K.J. Cook, E.C. Simpson, L.T. Bezzina, M. Dasgupta, D.J. Hinde, K. Banerjee, A.C. Berriman, C. Sengupta, Phys. Rev. Lett. **122**, 102501 (2019)

[20] C. Joshi, H. Kumawat, R. K. Singh, N. L. Singh, D. Patel, B. K. Nayak, J. Acharya, A. Parihari, K. Rani, S. D. Sharma, G. Kaur, I. Ahmed, K. S. Golda, N. Saneesh, Kumar, A. Jhingan , P. Sugathan, Eur.Phys.J. A 57, 40 (2022).

[21] http://www.iuac.res.in/elab/das/ppdas/Tutorials/fuman.html (2020)

[22] A. Chatterjee, LAMPS: Linux Advanced Multiparameter System (2008), http://www.tifr.res.in/~pell/lamps.html

[23] I. J. Thompson, FRESCO:version FRES 3.1 (2019), http://www. fresco.org.uk/source/fres-v31.html

[24] A. Winther, Nucl. Phys. A **572**, 191 (1994).

[25] D. Patel, S. Mukherjee, D.C. Biswas, B.K.Nayak,Y.K.Gupta, L.S. Danu, S. Santra, E.T. Mirgule, Phys. Rev. C **91**, 054614 (2015)

[26] M.S. Hussein, P.R.S. Gomes, J. Lubian, L.C. Chamon, Phys. Rev. C **73**, 044610 (2006)

[27] A. Diaz-Torres, I.J. Thompson, C. Beck, Phys. Rev. C **68**, 044607 (2003).

[28] P.R.S. Gomes, J. Lubian, I. Padron, R.M. Anjos, Phys. Rev. C 71 (2005) 01760

[29] P. Amador-Valenzuela, A.E.F. Martinez-Quiroz, D. L, J.C. MR, J.Phys. Conf. Ser. **876**, 012002 (2017)

[30] N.Keeley,K.W.Kemper, K. Rusek, Phys.Rev.C**65**, 014601 (2001)

[31] P.R.S. Gomes, M.D. Rodríguez, G.V. Martí, I. Padron, L.C. Chamon, J.O. Fernández Niello, O.A. Capurro, A.J. Pacheco, J.E. Testoni, A. Arazi et al., Phys. Rev. C **71**, 034608 (2005)

[32] T. Wada, Nucl. Phys. A **307**, 425 (1978)

[33] P. Mohr, D. Galaviz, Z. Fulop, G. Gyurky, G.G. Kiss, E. Somorjai, Phys. Rev. C **82**, 047601 (2010)

[34] M. Dasgupta *et al.*, Nucl. Phys. A **834**, 147c (2010).

[35] M. Dasgupta *et al.*, Phys. Rev. Lett. **82**, 1395 (1999).

[36] D. C. Biswas, R. K. Choudhury, D. M. Nadkarni, and V. S. Ramamurthy, Phys. Rev. C **52**, 2827 (1995).

[37] D. C. Biswas, R. K. Choudhury, B. K. Nayak, D. M. Nadkarni, and V. S. Ramamurthy, Phys. Rev. C **56**, 1926 (1997).

[38] P.R.S. Gomes, J. Lubian, B. Paes, V.N. Garcia, D.S. Monteiro, et al., Nuclear Physics A **828,** 233–252 (2009).